On the Efficiency Limits and Electric Field Stresses of Wireless Charging for Electric Buses: A 50-kW Experimental Study Based on Opportunity Charging

Calvin Riekerk, *Graduate Student Member, IEEE*, Wenli Shi, *Member, IEEE*, Gangwei Zhu, *Member, IEEE*, Jianning Dong, *Senior Member, IEEE*, Thiago Batista Soeiro, *Senior Member, IEEE*, and Pavol Bauer, *Senior Member, IEEE*

***Abstract*—Inductive power transfer (IPT) presents a promising solution for opportunity charging of electric buses. However, achieving an optimal balance between pad area, power transfer efficiency, and misalignment tolerance remains a significant challenge. This article explores the tradeoffs between power transfer efficiency and area-related power density and investigates the electric field distribution in the charging pads of wireless charging systems. The design requirements are first established. Based on these, a multiobjective optimization (MOO) framework is developed to address insulation constraints and current density limitations within the windings. The resulting Pareto front reveals that lower area-related power densities correspond to reduced efficiency, highlighting a fundamental design tradeoff. Furthermore, the study identifies critical regions within the charging pads that are the most susceptible to insulation failure. A 50-kW prototype was implemented and tested, with experimental results showing a dc–dc power efficiency ranging from 97.165% to 96.824% under 100-mm *X* and *Y* misalignment, and a stray field of 13.86 μT.**

***Index Terms*—DC–dc efficiency, electric buses, inductive power transfer (IPT).**

NOMENCLATURE

$\hat{H}_{\text{ext}}$	External magnetic field strength per turn.
$\hat{I}$	Peak value of the current through the charging pad.
ω_0	Angular resonance frequency.
subscript	$i = 1, 2$ stands for Tx and Rx sides, respectively.
$\tan(\delta)$	Dissipation factor of the capacitor.
B	Magnetic flux density.
C_{i}	Compensation capacitor in a S–S-compensated system.
d_a	Diameter of the strand of the Litz wire.
E	Electric field at surface boundary.
f	Operating frequency.
I_i	Root-mean-square value of the charging pad current.
J	Induced current amplitude.
k	Coupling coefficient between the charging pads.
L_{i}	Self-inductance of the charging pad.
l_{coil}	Length of the Litz wire for the charging pad.
M	Mutual inductance between the charging pads.
n_{str}	Number of strands of the Litz wire.
$P_{\text{cap},i}$	Resonant capacitor loss.
$R_{\text{ac},i}$	AC resistance of the charging pad.
r_{dc}	DC resistance per unit length per unit strand of the Litz wire.
V_{dc}	DC voltage at the output.

Received 1 August 2025; revised 24 October 2025; accepted 2 November 2025. Date of publication 10 November 2025; date of current version 4 June 2026. This project has received funding from the Electronic Components and Systems for European Leadership Joint Undertaking under grant agreement No. 876868. This Joint Undertaking receives support from the European Union's Horizon 2020 research and innovation programme and Germany, Slovakia, Netherlands, Spain, Italy. Recommended for publication by Associate Editor Herbert Ho-Ching Iu. *(Corresponding author: Calvin Riekerk.)*

Calvin Riekerk, Wenli Shi, Jianning Dong, and Pavol Bauer are with the Faculty of Electrical Engineering, Mathematics and Computer Science, Delft University of Technology, 2628 CD Delft, The Netherlands (e-mail: C.Riekerk@tudelft.nl; W.Shi-3@tudelft.nl; J.Dong-4@tudelft.nl; P.Bauer@tudelft.nl).

Gangwei Zhu is with the Department of Electrical Engineering, City University of Hong Kong, Hong Kong (e-mail: gangwzhu@cityu.edu.hk).

Thiago Batista Soeiro is with the Faculty of Electrical Engineering, Mathematics and Computer Science, University of Twente, 7522 NB Enschede, The Netherlands (e-mail: t.batistasoeiro@utwente.nl).

Color versions of one or more figures in this article are available at https://doi.org/10.1109/JESTPE.2025.3631233.

Digital Object Identifier 10.1109/JESTPE.2025.3631233

I. INTRODUCTION

ELECTRIFICATION of buses helps reduce CO_2 emission brought by public transportation. Trolley buses have been a good example of this. They can electrify public transport, while relieving the worries of limited driving range. However, there are some limitations to using this technology. The trolley grid infrastructure limits the flexibility of the bus route, as the overhead lines only allow the trolley bus to drive. Furthermore, the overhead lines cause visual pollution. Opportunity charging can overcome these limitations without driving range issues, as the electric bus would be able to charge its battery at bus stops while the passengers hop in/off.

The state-of-the-art opportunity charging is currently implemented through metal contacts, which could wear down fast due to weather effects and mechanical fatigue. The inductive power transfer (IPT) technology shown in Fig. 1 could solve the problem as it uses the magnetic field to charge the bus in a contactless manner. This results in no mechanical contact between the charger and the vehicle, which means higher

TABLE I
SPECIFICATIONS OF THE STATE-OF-THE-ART IPT SYSTEMS

References	Rated power [kW]	Year	Airgap [mm]	Operating frequency [kHz]	DC link voltage Tx/Rx [V]	Modules	Area power density [kW/m^2]	Efficiency Aligned -Misaligned [%]
KAIST [4]	100	2014	260	20	500/350	5x20 kW receiver (dynamic charging)	N/A	80.8-N/A (DC-DC)
KRRI [8]	818	2015	50	60	2667/2800	4x200 kW receiver (dynamic charging)	N/A	82.7-N/A (DC-DC)
WAVE [9]	50	2015	178	23.4	350 (Nominal load side)	1x50 kW	N/A	92-N/A (DC-DC)
University of Seoul [10]	150	2016	70	60	767.6/743.6	1x150kW	781.2	90.44-N/A (DC-DC)
Fraunhofer [11]	22	2015	136	100	800/425	1x20 kW	61.1	91-89 (Grid to Battery, 120/0 mm)
New York University [12]	25	2016	210	85	750/375	1x25 kW	N/A	91-N/A (Grid to Battery)
ETH Zürich [13]	50	2016	160	85	800/800	1x50 kW	160	95.8-92 (DC-DC, 150/0 mm)
IPT Technology [14]	100	2018	150	N/A	N/A	2x50kW receiver	N/A	93-N/A (N/A)
InductEV [5]	200	2019	178	20	500 (Nominal load side)	4x50 kW	N/A	90-N/A (Grid to Battery)
Chalmers University of Technology [15]	50	2020	140	85	800/800	1x50 kW	290.7	96.6-N/A (DC-DC)
ORNL [16]	50	2021	150	85	500/500	1x50 kW	195	94.35-88.5 (DC-DC, 100/0 mm)
ORNL [17], [18]	20	2021	280	22	800/370	1x20 kW	31.9	96.21-N/A (DC-DC)
Zhejiang University [19]	50	2021	160	85	885/593	2x15, 1x20 kW	208	95.2-N/A (DC-DC)
TU Delft [20]	20	2022	150	85	750/800	1x20 kW	69.1	97.2-94.1 (DC-DC, 150/0 mm)
University of Auckland [21]	50	2023	160	85	568/568	1x50 kW	133.3	95.8-93.7 (DC-DC, 75/100 mm)
Universidad Politécnica de Madrid [22]	37.4	2024	145	85	800/830	1x37.4 kW	302.0	96.72-96.35 (DC-DC, 50/50 mm)
TU Delft (this work)	50	2025	160	85	1250/1250	1x50 kW	86.5	97.16-96.82 (DC-DC, 100/100 mm)

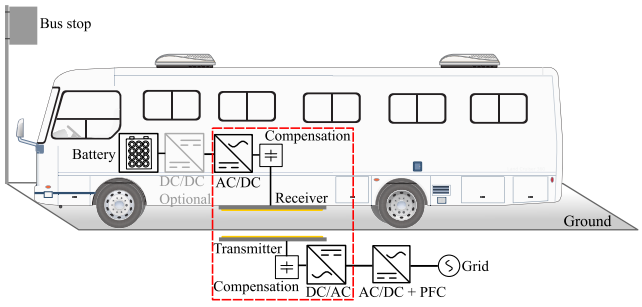

Fig. 1. Configuration of the electric bus opportunity charging system.

resiliency and less maintenance than conductive chargers. Several examples of both static and dynamic IPT charging have been tested in the field by [1], [2], [3], [4], [5], and [6]. However, the bus only has a short charging interval of up to several minutes at each bus stop, which means high-power charging is needed to transfer a significant amount of electrical energy to the battery. For example, assuming three minutes of charging at 50 kW, the charged energy is just enough to cover 1.9 km of range to reach the next charging stop based on the data given in [7].

Different companies and universities have developed several high-power IPT systems in the last decade. Table I presents a general overview of these systems. It can be seen that although there are multiple ≥ 50 kW systems reported in the literature, there is still space to improve the system efficiency when compared with pantographs. Commercial pantograph chargers can reach an efficiency of 94%–96% [23]. Even though IPT provides other advantages, more work is still necessary to compete with these chargers.

Most designs in Table I mainly focus on power density while keeping an acceptable efficiency. This makes a lot of sense considering the limited space under a car. Although a trolley bus provides significantly more space compared to a

car, allowing for a larger Rx charging pad compared to the ones meant for a regular car, the power density, efficiency, and misalignment are still relevant metrics considering the limited charging time. Another point worth mentioning is that as a heavy-duty vehicle, the trolley bus usually needs a dc-bus voltage of 600–750 V [24]. However, there is consideration to increase the dc link voltage to 1200 V for heavy-duty EVs to reduce current stress and losses in the IPT system [25]. However, there is a lack in the design and practical implementation of the IPT system for high dc-bus voltage in existing work.

The performance metrics of a high-power IPT opportunity charging system, including power transfer efficiency, are limited by several design challenges.

1) *Tradeoff Between Pad Area and Power Transfer Efficiency:* In the design of wireless power transfer systems, especially for electric vehicles, engineers often face a critical tradeoff between pad area and power transfer efficiency. By applying multiobjective optimization (MOO), this tradeoff is elegantly captured in the Pareto front, a graphical representation that illustrates the optimal balance between competing objectives [13], [20], [26].
   Each point on the Pareto front represents a design that achieves the maximum possible efficiency for a given power density. In other words, no design on the front can improve in one metric (efficiency or power density) without compromising the other. This makes the Pareto front a powerful tool for evaluating and selecting design strategies based on specific application needs.
   Meanwhile, the Pareto front also reveals underlying physical limitations. As power density decreases, efficiency initially improves but only up to a point. Beyond this threshold, further reductions in power density do not yield significant gains in efficiency as shown in [13], [20], and [26].
2) *Insulation-Related High Voltage Stress in Components:* The ac voltage in the resonant tank of the IPT system is usually several times higher than the dc voltage, which brings substantial voltage stresses in the compensation components and windings. While the voltage stress in the capacitor can be partially alleviated using the integrated solution as in [20], insulation of winding wire, space between turns, and between the winding turns and ferrites have to be carefully chosen to avoid insulation failure caused by locally concentrated electric field as studied in [27].

To address the aforementioned challenges, MOO is employed to derive and interpret the Pareto front. The resulting design solutions offer valuable insight into the geometric configuration of the charging pads. Various methodologies for implementing MOO have been extensively discussed in the literature, including works such as [13], [20], [26], [28], and [29]. Based on the identified challenges and the reviewed literature, the following research gaps remain.

1) Although larger coil geometries theoretically allow for improved coupling and power transfer, it remains unclear why efficiency plateaus or diminishes along the Pareto front, especially for the trolley bus application, where the area limit is not as stringent as passenger cars.
2) Guidelines for designing and the practical implementation of high-power IPT systems for EVs with high-voltage powertrains are not yet sufficiently presented.

To fill the research gaps mentioned above, this article explores the limits of efficiency with increased charging pad area. The following contributions are made.

1) Identifying the design requirements, design space, and physical boundaries and implementing an MOO routine to explore the design of the wireless opportunity charging system for trolley buses.
2) Providing insights and understanding of the limits between power transfer efficiency and area-related power density by implementing an MOO routine.
3) Investigating the electric field distribution in the charging pads and providing guidelines to mitigate electric field stresses for high voltage IPT systems.
4) Verifying the methodology and the conclusions with a 50-kW prototype.

The article is organized in the following way. The loss modeling of an S–S-compensated IPT system is described in Section III. Additionally, the wire placements for the bifilar winding and electric field stresses are also studied in Section IV. Furthermore, the design process utilizing the MOO is also demonstrated to create a Pareto front for 50-kW IPT systems. In Section V, the developed 50-kW IPT system is presented and its functionality is verified. The conclusion is provided in Section VI.

II. Design Requirements for Opportunity Charging

To better understand the necessary system specifications of the IPT system, a simulation was conducted focusing on charging power, battery weight, and charging time. This simulation is based on data from the trolleybuses in Arnhem, the Netherlands. Using the model in [30], the total energy per trip and the minimum required energy between stops were determined. According to the model, a total energy of 70.6 kWh is necessary for a single trip with 27 stops. The maximum required energy between two stops is 10.77 kWh. It is assumed that the specific energy of the battery is 180 Wh/kg and the SOC range is between 20% and 85%. Based on this case, the charging time per stop is calculated as follows:

$$t_{\text{charge}} = \frac{E_{\text{tot}} - M_{\text{bat}} \cdot \text{SPe} \cdot \text{dSOC}}{n \big/ \left(3600 P_{\text{charge}}\right)}. \tag{1}$$

The results for this route are shown in Fig. 2. As illustrated, the dashed green lines represent a charging time between 30 and 60 s, which is an acceptable waiting time at each stop for passengers to board. The gray area indicates the working plane where the battery capacity is insufficient to provide the necessary energy for the bus to travel between the most

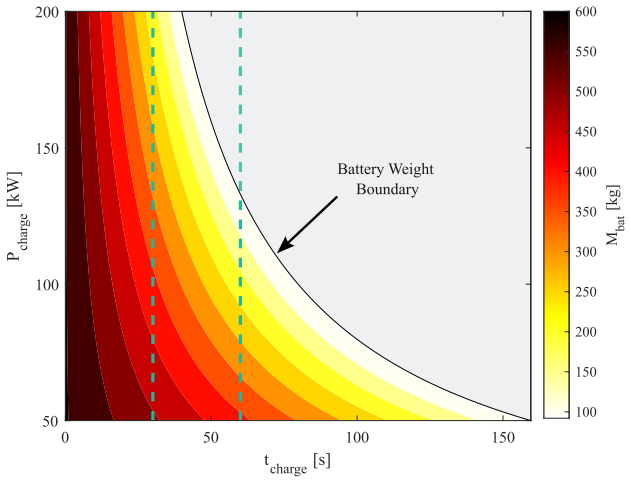

Fig. 2. Simulation of the charging time per stop versus the charging power for different battery weights. The dashed green lines represent an acceptable charging time of 30–60 s. The minimum required battery weight between the two furthest stops limits the battery weight boundary.

energy-consuming sections of the route. For a single trip on this route, a battery weight of 600 kg is required without any charging at stops. With a charging time of 30 s, a reduction in battery weight of nearly 17% can be achieved at a charging power of 50 kW. This reduction could be further increased to 60% if a charging power of 200 kW is utilized.

A. Specifications for the IPT Charger

The simulation results indicate that a higher power charging level significantly reduces the battery weight of the bus. Additionally, extending the charging time can further decrease the necessary weight. However, as mentioned in the introduction, designing an IPT system with such a high power level is challenging due to the limitations imposed by high current through the windings. This challenge is compounded by the low voltage boundary for dc, which is set at 1500 V. Operating within the low-voltage region simplifies the manufacturing process. Moreover, opting for higher power systems increases the risk of insulation issues in the charging pads.

Based on the discussion in the introduction, the design requirements of the considered conversion stage for opportunity charging are elaborated as follows.

1) The rated power of each charging module should be ≥ 50 kW to minimize waiting time at stops.
2) The power density of the charging pads should be high enough to fit multiple charging pads underneath the body part of an electric bus.
3) The designed airgap will be at least 150 mm. This is according to the HD Z2 class in [31].
4) The system needs to be misalignment-tolerant. According to the heavy-duty vehicle standard [31], a 100-mm X and Y offset must be tolerable.
5) The efficiency of the IPT system should be as high as possible to reduce the thermal stress in components, so that less maintenance is needed for the cooling system and a longer lifetime is achieved.

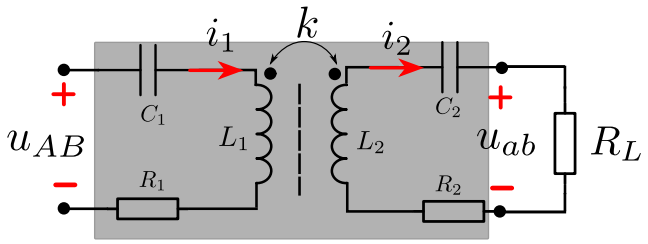

Fig. 3. S–S-compensated IPT system.

6) The dc-bus voltage should be ≥ 800 V to reduce current stress in wires and make it easier to choose wire specifications.
7) The insulation clearance between subcomponents in the charging pads should be sufficient to withstand voltage stresses.
8) The wire arrangement should be carefully studied to pursue the best tradeoff between efficiency and power density.

III. Analytical Modeling of an IPT System

A. Efficiency Maximization

As the specifications are set in Section II-A, it is time to start working on the model necessary for the MOO. The S–S compensation presented in Fig. 3 is chosen for this work because of its simplicity. Furthermore, its design allows for a higher peak efficiency [20], [32].

The maximum transmission efficiency for S–S compensation is limited by the figure of merit (FOM) [33]

$$\text{FOM} = kQ_{\text{coils}} \tag{2}$$

where the coupling factor (k) and the quality factor (Q_{coils}) are given by

$$k = \frac{M}{\sqrt{L_1 L_2}} \tag{3}$$

$$Q_{\text{coils}} = \sqrt{Q_1 Q_2} = \sqrt{\frac{\omega_0^2 L_1 L_2}{R_{\text{ac},1} R_{\text{ac},2}}}. \tag{4}$$

It is clear that a low ac resistance is beneficial for the quality factor according to (4). So, for an S–S-compensated system, maximizing k and Q_{coils} is important for the highest possible efficiency.

Furthermore, it is necessary to operate at the optimal load. The required mutual inductance to operate at the optimal load is

$$M = \frac{8}{\pi^2} \frac{V_{\text{dc}}^2}{\omega_0 P_{\text{out}}} \sqrt{\frac{R_{\text{ac},1}}{R_{\text{ac},2}}}. \tag{5}$$

Operating at the optimal load ensures that the losses in resistances of the charging pads and resonant capacitors are minimized [26].

B. Power Loss Models

The power loss calculation is crucial to obtain the dc–dc efficiency of the IPT system. The dc and skin effect losses in the Litz wire of the pads can be computed using [33]

$$P_{\text{skin}} + P_{\text{dc}} = n_{\text{str}} r_{dc} F_R(f) \left(\frac{\hat{I}}{n_{\text{str}}}\right)^2 l_{\text{coil}} \tag{6}$$

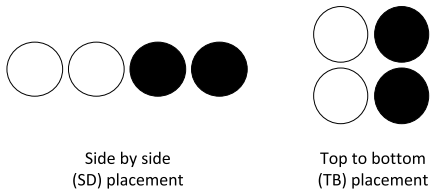

Fig. 4. Possible wire placements: side by SD and TB (the coloring indicates if they are part of the same turn).

where F_R is a factor [34] dependent on the frequency and the strand diameter.

The losses due to the internal proximity effect in the charging pad can be determined by [33]

$$P_{\text{prox,int}} = n_{\text{str}} r_{dc} G_R(f) \frac{\hat{I}}{2\pi^2 d_a^2} l_{\text{coil}} \tag{7}$$

where G_R is a factor dependent on f and d_a is the diameter of the Litz wire.

The external proximity effect caused winding loss can be calculated as

$$P_{\text{prox,ext}} = \sum_{i=1}^{N} n_{\text{str}} r_{dc} G_R(f) \int_{l_i} \hat{H}_{\text{ext}}(l)^2 \, dl. \tag{8}$$

The external proximity effect loss is evaluated for each turn because the external magnetic field for each turn differs. The ferrite core loss is approximated using the Steinmetz equation

$$P_{\text{core}} = \int_{V_{fe,i}} k_{fe} f^{\alpha} B^{\beta} \, dV \tag{9}$$

where k_{fe}, α, and β are the Steinmetz parameters of the core material. For the chosen core material 3C95, $k_{fe} = 92.66$, $\alpha = 1.045$, and $\beta = 2.44$ [35].

The loss caused by the eddy currents in the magnetic shielding is given by

$$P_{\text{sh},i} = \int_{V_{\text{sh},i}} \frac{\mathbb{R}(\boldsymbol{J} \cdot \boldsymbol{E}^*)}{2}, \quad dV. \tag{10}$$

The resonant capacitor loss for an S–S-compensated system is

$$P_{\text{cap},i} = I_i^2 \frac{\tan(\delta)}{\omega_0 C_i}. \tag{11}$$

The dissipation factor $\tan(\delta)$ is dependent on the kind of capacitor and the operating frequency. Higher operating frequencies will result in higher dissipation factors, which would negatively affect the capacitor loss as shown in (11).

IV. Charging Pad Analysis

A. Bifilar Winding

As mentioned in Section II-A, the need for substantial winding currents arises in high-power applications. However, this requirement often results in the usage of thick Litz wire, which can be costly and may not always be readily accessible in the market. The high-power problems require a solution for the winding. Bifilar windings could solve this by increasing their current density. Two possible configurations are shown in Fig. 4. These two configurations will be compared in this section in terms of efficiency, assuming that: 1) both placements have the same specifications except for the turn gap to ensure the same coil spread and 2) the gap between the top and bottom wire is the same as the turn of the SD placement. This work is limited to bifilar configurations. Trifilar or quadfilar configurations are avoided, as they would significantly increase the overall area of the charging pads when using the SD configuration. Alternatively, employing the TB configuration would complicate the construction process due to the need for additional layers. In addition, transposing may be necessary due to imbalance issues between the windings.

TABLE II
Parameters of the Bifilar Winding Placements

	L_1 [μH]	L_2 [μH]	k	V_{in} [V]	V_{out} [V]	η
SD	163.45	148.49	0.329	1312.42	1287.82	97.71
TB	157.92	142.36	0.320	1270.31	1246.41	97.65

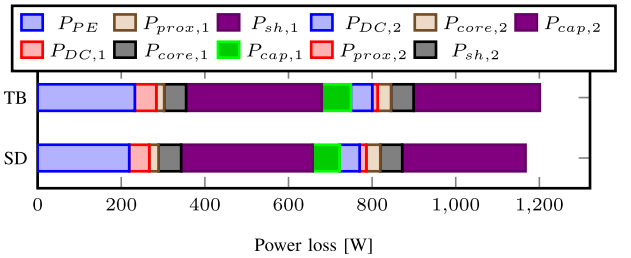

Fig. 5. Loss comparison of the SD and TB bifilar placement at 50 kW.

The following procedure is used to estimate the efficiency of each design.

1) The specifications of Table II are obtained from an FEM simulation-based MOO routine, which will be presented later in Section IV-C.
2) Obtain the compensation capacitance.
3) The dc voltage at the load side is calculated to fulfill the optimal load condition.
4) Based on the optimal load, it is possible to compute the current and voltage in the IPT system utilizing KVL.
5) Compute the losses using (6)–(11) and the shielding loss (10) using FEM.

The results are shown in Fig. 5, computed using the equations provided in Section III and the FEM field results. This indicates that the side-by-side (SD) placement has a higher coupling factor and self-inductance than the top-to-bottom (TB) placement due to the wires being overall closer to the other charging pad. This results in a higher current and a lower voltage for TB, which increases the losses except for the switching, core, and proximity loss. The lower dc link voltage causes lower switching loss. A larger turn gap for TB results in a lower magnetic field penetration into the wires and core. Furthermore, the same conclusion can be seen from the FOM in which the SD placement outperforms the TB placement.

B. High-Voltage Electric Field Stresses

The electric field generates significant stresses between the winding wire and ferrite core, particularly at higher power

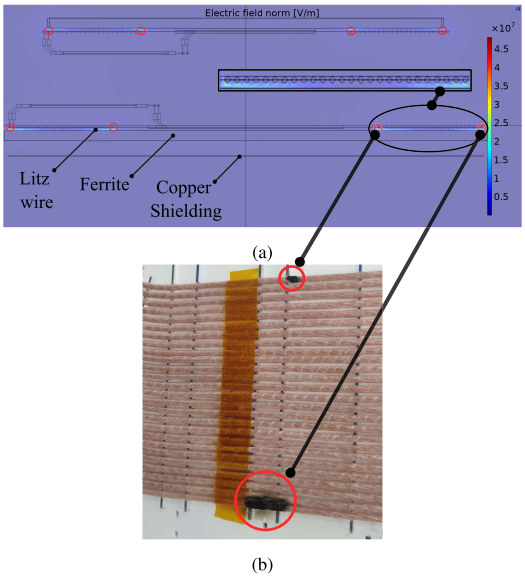

Fig. 6. Electric field stresses between the windings and ferrite using (a) simulation, which shows the weak spots (using the red circles) and (b) photograph showing breakdown test results (the red circles show the highly concentrated electric field spots).

levels as referred to in Section II-A. The relative real permittivity of the ferrite 3C95 is in the order of 10 [36]. The high permittivity results in a higher electric field at the sharp edges of the ferrite bars due to the small curvature. Minimizing the impact of this emission is crucial to prevent insulation failure, for example, as shown in Fig. 6(b).

The weak spots are identified through an FEM electric field simulation and a breakdown test. The results are shown in Fig. 6. The simulation from Fig. 6(a) indicates that the innermost turn and the turn nearest to the end of the ferrite bar are the most vulnerable to insulation failure, as indicated by the red circles. This is attributed to the high potential difference occurring at these specific turns. Furthermore, they are also the edge of the winding, which is where the edge effect is prominent [37]. This conclusion aligns with observations from tests in Fig. 6(b), where the insulation is consistently compromised at these locations. In the high-field regions, a peak electric field of around 18 kV/mm is observed. According to [38], air has a dielectric strength of approximately 2 kV/mm, and the insulation on the Litz wire is rated for 2 kV_{peak}. Based on these values, the following guideline for insulation thickness is used:

$$T_{\text{insulation}} = \frac{E_{\text{coil}} d_{cf}}{E_{\text{insulation}}} \tag{12}$$

where $T_{\text{insulation}}$ is the total thickness of the insulation material, E_{coil} is the peak electric field, d_{cf} is the distance between coil and ferrite, and $E_{\text{insulation}}$ is the dielectric strength of the insulation material. For prototyping purposes, Kapton tape was used to implement reinforced insulation. However, for professional and industrial applications, epoxy resin is a more robust and effective solution for insulation.

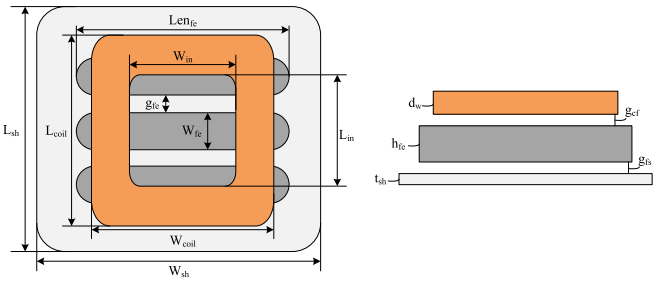

Fig. 7. Charging pad design including design variables.

C. Multiobjective Optimization

The improvements discussed in Sections IV-A and IV-B, including the specification from Section II-A, have been applied to the MOO framework presented in [20] and [26]. They present a hybrid method which involves FEM to solve the magnetic field, while the analytical equations in (6)–(9) are applied to compute the losses. The windings are modeled as a 3-D homogeneous multiturn coil block with uniform current density. This means that the losses regarding the charging pads, such as the skin-effect and proximity-effect losses, need to be modeled using the solved magnetic field for each turn of the coil and empirical equations. The optimization objectives are to maximize the following.

1) The power transfer efficiency.
2) The receiver pad area-related power density.
3) The gravimetric power density.

It is chosen to run the MOO for 85 kHz as this is the most commonly used frequency in Table I. The SD turn placement is selected because of its excellent FOM. Furthermore, the dc link voltage is limited to 1400 V to create a safety margin and to keep the system in the LV dc voltage market. The constraint for the charging pad area is chosen so that four charging pads fit under a BYD K9S bus, which are similarly placed as the opportunity charger in [5]. According to the heavy-duty vehicle standard presented in [31], the air gap between the charging pads is set to 150 mm. To ensure proper functioning, the minimum clearance between the coil and the ferrite, as well as between the ferrite and shielding, is chosen to be 0.1 mm. The required time to evaluate a complete design varies between 3 and 6 min (Intel[1] Xeon[1] W-2223 CPU at 3.60 GHz, 16,0 GB RAM).

The optimization variables are given in Table III which are illustrated in Fig. 7.

The relative ferrite length is equal to

$$\text{Len}_{fe} = \frac{\text{Len}_{fe,r} W_{\text{coil}}}{100} \tag{13}$$

where $g_{fe,r}$ is given by

$$g_{fe,r} = \frac{g_{fe}}{100} \frac{W_{\text{coil}} - N_{fe} W_{fe}}{N_{fe} - 1}. \tag{14}$$

The MOO makes use of the particle swarm optimization (PSO) algorithm, which allows for a more diverse swarm to avoid a local optimum [39]. The three above-mentioned

[1]Registered trademark.

TABLE III
OPTIMIZATION VARIABLES AND THEIR RANGE USING BIFILAR WINDING

Variable	Symbol	Unit	Range
Number of turns	N	-	10-45
Diameter of Litz wire	d_w	mm	4.15-5.60
Inner width of coil	W_{in}	mm	100-600
Inner length of coil	L_{in}	mm	100-600
Gap between turns	g_{turn}	mm	4-15
Ferrite width	W_{fe}	mm	15-45
Ferrite height	H_{fe}	mm	5-35
Relative ferrite length	$Len_{fe,r}$	%	10-100
Number of ferrite bars	N_{fe}	-	3-15
Relative gap between ferrite	$g_{fe,r}$	%	10-100
Gap between coil and ferrite	g_{cf}	mm	0.1-10
Gap between ferrite and shielding	g_{fs}	mm	0.1-50

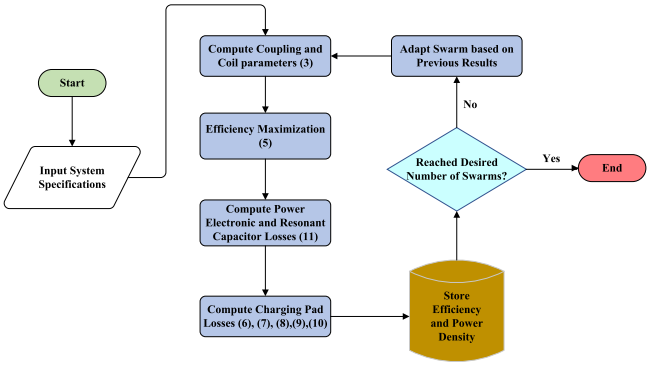

Fig. 8. Flowchart of the optimization process used to design an IPT system.

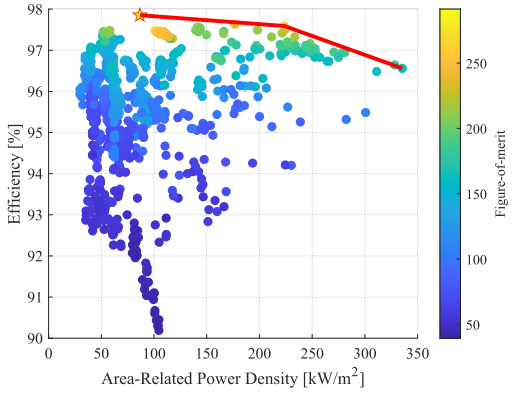

Fig. 9. Pareto front obtained from the MOO between the efficiency and area-related power density with the color indicating the FOM at 85 kHz (evaluated designs = 915).

TABLE IV
DESIGN PARAMETERS OF THE MARKED IPT SYSTEM DESIGN IN FIG. 9

Parameter	Value
L_1 [μH]	169.75
L_2 [μH]	152.75
k	0.33
$V_{in,DC}$ [V]	1348
$V_{out,DC}$ [V]	1323
$\hat{I}_1$ [A]	59.52
$\hat{I}_2$ [A]	60.43
$R_{AC,1}$ [Ω]	0.1083
$R_{AC,2}$ [Ω]	0.0845
η	0.9785
FOM	291

objectives are used to achieve the Pareto front, which is studied later for the final design. The overall design procedure of the MOO is shown in Fig. 8.

The first step is to input the system specifications. These include the requirements set in [31], which include the air gap and rated power. Furthermore, a range in the optimization variables is set as shown in Table III. After inputting the system specification, the swarm is created, which consists of a population count of 15. The swarm is either randomized if it is the first swarm or adapted based on the optimization results of the previous swarms. So, the MOO does not sweep through all design parameters in Table III with brutal force.

For every design, it is necessary to execute the outlined steps, where each step aligns with the blue blocks depicted in Fig. 8: 1) model the design in FEM to obtain the self and mutual inductances; equations (3) and (5) are used to get the coupling. The area and weight are also computed in this step; 2) apply KVL to the equivalent circuit to calculate the input current and voltage using (15) and (16). Check if the design exceeds the dc link voltage requirement. In the case that it exceeds the limit, it will skip to the next design in the swarm; 3) retrieve the losses in the capacitors and the H-bridge converters; and 4) compute the dc coil losses and ac-related losses using (6)–(8), the ferrite loss with (9), and extract the shielding loss from FEM based on (10)

$$I_1 = \frac{z_2 I_2}{z_M} \tag{15}$$

$$V_1 = I_1 z_1 - z_M I_2. \tag{16}$$

With all the system losses, charging pad area, and weight computed, it is possible to obtain the system efficiency and the power density. The efficiency and power density of the swarm will be used to determine the input variables of Table III. Now that all the swarms are computed, the Pareto front can be created, which is shown in Fig. 9. A final design marked by the yellow star in Fig. 9 is chosen because it is the most efficient design found by the MOO, where four modules would fit under a BYD K9S. Additionally, the design also has the highest FOM. The final design parameters marked by the yellow star are shown in Tables IV and V.

As shown in Fig. 9, the Pareto front terminates at relatively low area-related power densities, consistent with observations in [13], [20], and [26]. Typically, the Pareto front should extend toward lower power densities while increasing efficiency, illustrating the tradeoff between efficiency and power density. However, no design has been able to maintain this trend, as shown in Fig. 9. Two factors play a crucial role: the optimal load condition and bifurcation. One reason is that we design systems to avoid bifurcation to ensure zero voltage switching (ZVS). A system enters bifurcation according to the following equation:

$$k > k_{\text{crit}} = \frac{R_{\text{Lac}}}{\omega_0 L_2}. \tag{17}$$

TABLE V
FINAL DESIGN OF 85 KHZ OBTAINED FROM THE MOO

Variable	Symbol	Unit	Tx	Rx
Number of turns	N	-	13	11
Inner width of coil	W_{in}	cm	29.572	33.666
Inner length of coil	L_{in}	cm	42.56	55.654
Outer width of coil	W_{coil}	cm	76.98	65.82
Outer length of coil	L_{coil}	cm	63.988	87.81
Gap between turns	g_{turn}	mm	1.8	2.6
Ferrite width	W_{fe}	cm	4.32	4.32
Ferrite height	H_{fe}	cm	1.64	1.64
Ferrite length	Len_{fe}	cm	78.12	64.17
Number of ferrite bars	N_{fe}	-	9	9
Width of shielding	W_{sh}	cm	76.98	65.82
Length of shielding	L_{sh}	cm	63.988	87.81
Gap between coil and ferrite	g_{cf}	mm	0.30	3.24
Gap between ferrite and shielding	g_{fs}	mm	23.92	48.88
Thickness of shielding	t_{sh}	mm	1	1
Number of strands	n_{str}	-	2205	2205
Strand diameter	d_a	mm	0.0711	0.0711

The maximum value of the optimal load (R_{Lac}) is constrained by the voltage and power level, as is the resonant frequency. Consequently, the only variable not limited is the self-inductance of the secondary charging pad, which increases with the area of the charging pad. This increase in L_2 reduces k_{crit}, making it challenging to find a design that avoids bifurcation.

Given that L_2 tends to be larger for coils with lower power density, the optimal quality factor product is achieved when $L_1 = L_2$. However, since the mutual inductance is constrained by the dc voltage limit, there are only two viable design strategies for large receiver coils: either reduce the coupling factor between the coils or decrease L_1.

Reducing L_1 would lower its quality factor, thereby diminishing the overall quality factor product. On the other hand, decreasing the coupling factor would eventually compromise the system's FOM given in (2). Therefore, a careful tradeoff must be made between maintaining high quality factors and preserving adequate coupling, while keeping the system out of bifurcation, especially at lower area-related power densities where it is expected to reach a higher efficiency.

The loss distribution is presented in Fig. 10. It shows that the capacitor losses are the most significant. There are several ways to reduce this, as presented in (11), but they all come with a tradeoff.

1) Employing capacitors with lower dissipation factors can reduce losses. In this design, customized film capacitors have already been utilized to maximize efficiency. While alternatives such as multilayer ceramic capacitors (MLCCs) may offer improved performance, they introduce challenges, including increased cost, a higher number of soldering points, and reduced system reliability.
2) Increasing the compensation capacitor value is constrained by the self-inductance of the charging pads and the operating frequency. This typically necessitates a reduction in coil size, which may adversely affect the efficiency and increase losses in the charging pads.

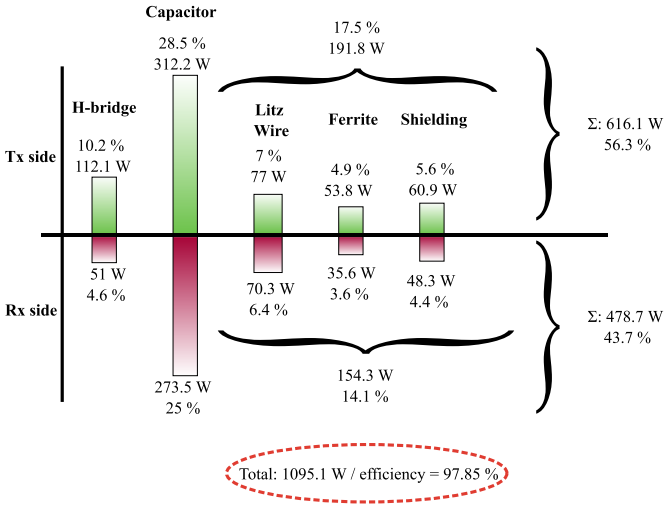

Fig. 10. Loss distribution of the 50-kW design.

3) Lowering the ac current is another potential approach; however, this is closely tied to the optimal load and the desired dc output voltage. Raising the dc voltage beyond 1500 V would classify the system as medium voltage, thereby complicating insulation design and increasing system complexity.

V. EXPERIMENTAL VERIFICATION

A. Experimental Setup

To validate the design obtained by the MOO, the 50-kW charging pads, H-bridge converters, and compensation capacitors are constructed. The circuit diagram and the prototype are shown in Fig. 11. The Tx charging pad, which has a similar build as the Rx charging pad, is shown in Fig. 12. The Litz wire utilized is the Efolit Litz wire from Elektrisola. An H-bridge converter is utilized at the Rx side to realize active rectification, which will increase total system efficiency compared to a conventional diode rectifier. The H-bridge converters make use of 1700-V SiC MOSFETs (G3R20MT17K). Three of these MOSFETs are connected in parallel to reduce the conduction losses. Customized capacitors from Celem are used with a voltage rating of 6000 Vrms and a capacitance of 21.65 and 22.95 nF for the Tx and Rx sides, respectively. The used Litz wire has a strand diameter of 0.071 mm and 2200 strands. The shielding material is copper to reduce the loss, as it is more conductive in exchange for slightly more weight. A circulating power test is used to attain the power demand of 50 kW. A Delta SM1500-CP-30 is utilized to supply the power losses. To measure the dc–dc efficiency, the WT500 power analyzer from Yokogawa is combined with two CT200 current transformers and a CT4072 differential probe from Cal Test Electronics. Two situations based on the heavy-duty vehicle standard [31] will be tested regarding the charging pad placement:

1) Aligned with an air gap of 160 mm.
2) Misaligned with an X and Y offset of 100 mm at an air gap of 160 mm.

The IPT system is tested with an air gap of 160 mm instead of 150 mm to make it comparable to other state-of-the-art

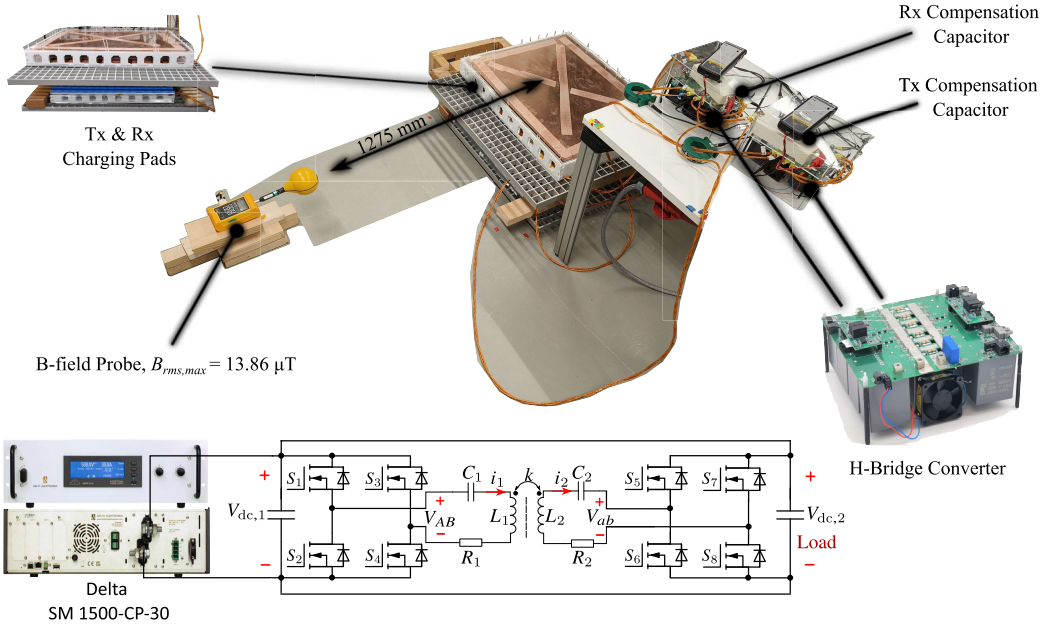

Fig. 11. 50-kW IPT system including schematic.

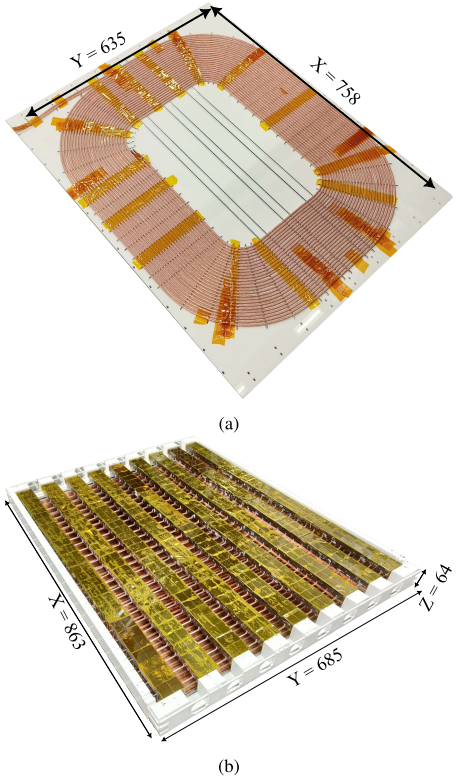

Fig. 12. (a) Tx charging pad coil and (b) ferrite and shielding.

systems. The comparison of the self-inductance and coupling between the theoretical design and the prototype at the two different testing situations is presented in Table VI. It is noteworthy that the drop in coupling at misalignment is not as pronounced. This occurs not solely due to the larger area of the charging pads, but also owing to the orientation of the charging

TABLE VI

SELF-INDUCTANCE AND COUPLING COEFFICIENT OF THE 50-KW SETUP AT ALIGNED AND MISALIGNED (X = 100 MM, Y = 100 MM) POSITIONS

	L_1 [μH]	L_2 [μH]	k
Aligned	163.23	141.45	0.31
Misaligned	158.56	143.47	0.26

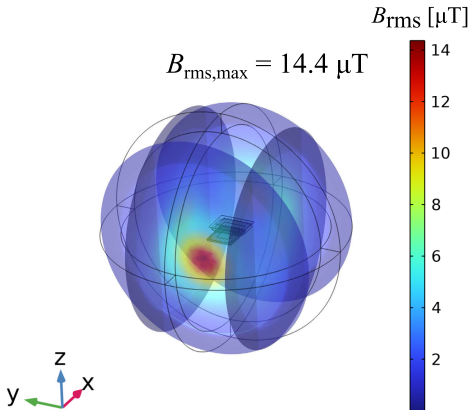

Fig. 13. FEM simulation of the 50-kW charging pads under 100-mm X and Y misalignment.

pads. From Table V, it can be observed that the Tx charging pad is wider than the Rx pad, and similarly, the length of the Rx charging pad is longer than the Tx pad. This means that with both X and Y offsets in place, a similar area is covered between the charging pads at misalignment corresponding to the results in Section IV-C.

Furthermore, the stray magnetic field was measured at a distance of 1275 mm under misaligned conditions. This measurement distance corresponds to Zone 2, as defined in [31], which represents the position of a person standing next

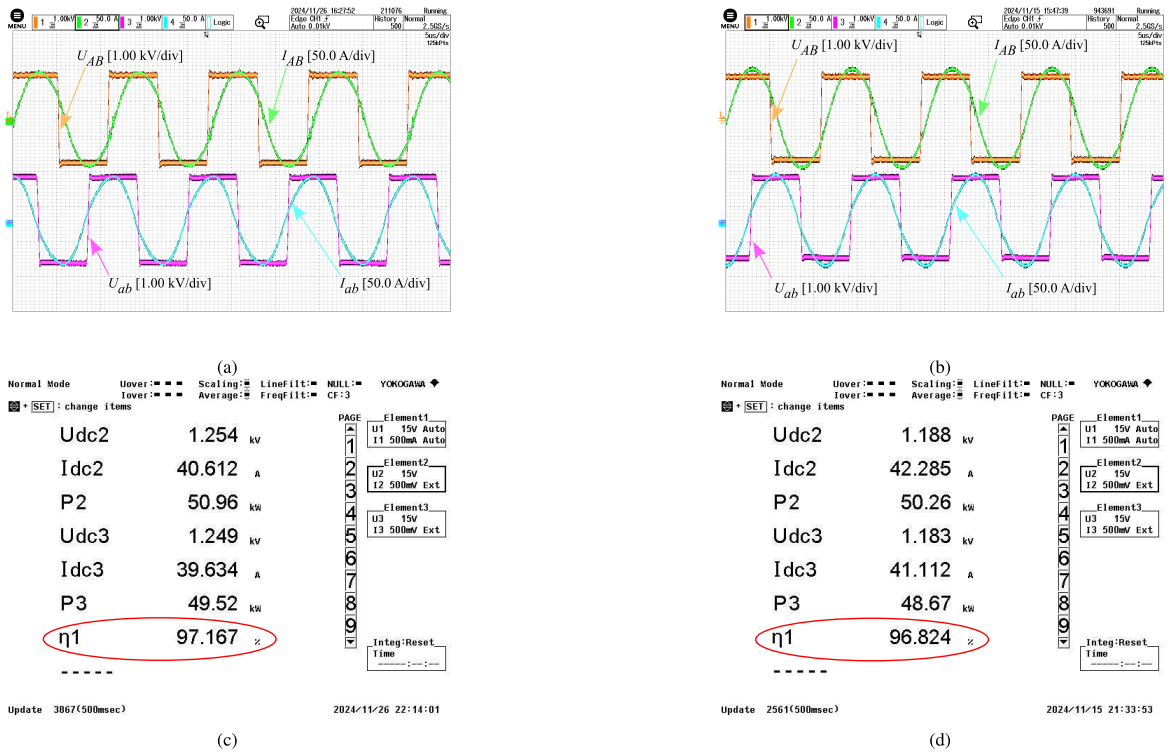

Fig. 14. (a) Measured waveforms at 160 mm, (b) measured waveforms at 160 mm with an X and Y offset of 100 mm, (c) dc–dc efficiency at 160 mm, and (d) dc–dc efficiency at 160 mm with an X and Y offset of 100 mm.

to the bus. The dimensions of the BYD K9S electric bus were used to determine this reference point. This means that the reference point needs to be at least half of the bus width. However, a conservative approach has been taken, so an extra safety margin has been added, which lands on 1275 mm [40]. Measurements were conducted under worst case misalignment conditions, as illustrated in Fig. 13. The FEA model shows that the maximum leakage flux in zone 2 next to where the bus would be located is 14.4 μT, which is lower than the 15 μT limit as defined in [31].

B. Results and Discussion

The measured waveforms of the ac voltage at the converter outputs and the ac current are shown in Fig. 14(a) and (b). It can be seen that V_{AB} leads I_{AB}, which would ensure ZVS turn-on for the Tx H-bridge MOSFETs. ZVS turn-on is also ensured at the Rx H-bridge converter as the current leads the voltage. The dc–dc efficiency is 97.167%, as pictured in Fig. 14(d). The trend of the efficiency at different power levels for both aligned and misaligned positions can be observed in Fig. 15. So, at lower power levels, the constant losses, such as switching losses, dominate. Especially as the turn-off current through the converter is still low, which could potentially result in hard switching. At higher power, the ohmic losses, such as the capacitor and dc + skin-effect losses, start to dominate as they scale quadratically with the current. Meanwhile, there will be sufficient turn-off current to ensure ZVS turn-on. A drop of only around 0.3% in the efficiency can be observed when misaligned, which is connected to the decrease in coupling shown in Table VI. Moreover, the system's misalignment

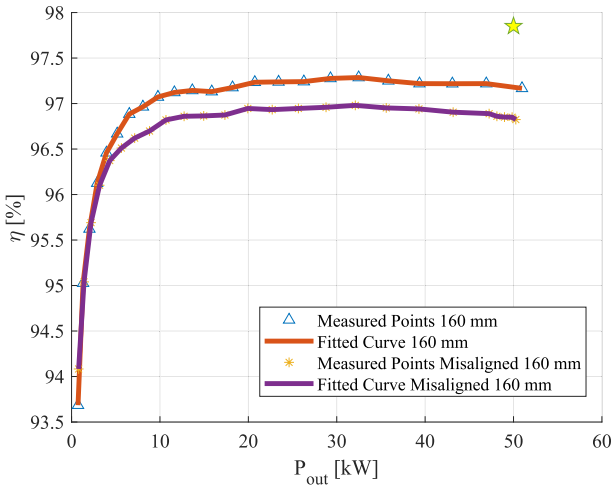

Fig. 15. Measured power transfer efficiency at different power levels, including the simulated dc–dc efficiency.

tolerance is proven to be good, as both efficiency curves are close to each other. As mentioned before, this is related to the orientation and size of the charging pads, which was also reflected in the small difference in the aligned and misaligned coupling. Fig. 11 also shows that the maximum measured magnetic leakage flux is 13.86 μT, which is within the CIED limit [31].

VI. Conclusion

This article provides a comprehensive analysis of the trade-offs between power transfer efficiency and area-related power

density in IPT systems for electric bus opportunity charging. An MOO framework was developed based on design requirements for opportunity charging, incorporating design constraints such as insulation limits and extended to support bifilar windings to accommodate high current requirements. Reinforcing the regions at the innermost turn and the turn nearest to the end of the ferrite bar is essential to mitigate the risk of insulation failure within the charging pads. The resulting Pareto front reveals a clear tradeoff between coupling coefficient and quality factor, particularly at lower area-related power densities, where bifurcation losses reduce overall efficiency.

A 50-kW IPT prototype was designed based on the MOO results and experimentally validated using a circulating power test. The system achieved a dc–dc efficiency of 97.167% under aligned conditions and 96.824% under 100-mm X and Y misalignment, while maintaining a stray magnetic field of 13.86 μT, which is well within safety limits.

These results validate the proposed design methodology and highlight the potential of achieving compact, efficient, and misalignment-tolerant IPT systems for high-power public transport applications.

ACKNOWLEDGMENT

The authors would like to thank Dr. Mohamad Ghaffarian Niasar for his valuable insights and expertise on high-voltage electric field stresses, which significantly contributed to the development of this work.

REFERENCES

[1] V. Cirimele et al., "The fabric ICT platform for managing wireless dynamic charging road lanes," *IEEE Trans. Veh. Technol.*, vol. 69, no. 3, pp. 2501–2512, Mar. 2020.

[2] J. Villa, J. Sanz, R. Acerete, and M. Perie, "Design considerations for WPT dynamic charging applications," in *Proc. AEIT Int. Conf. Electr. Electron. Technol. Automot. (AEIT AUTOMOTIVE)*, Jul. 2019, pp. 1–6.

[3] S. Laporte, G. Coquery, V. Deniau, A. De Bernardinis, and N. Hautière, "Dynamic wireless power transfer charging infrastructure for future EVs: From experimental track to real circulated roads demonstrations," *World Electr. Vehicle J.*, vol. 10, no. 4, p. 84, Nov. 2019. [Online]. Available: https://www.mdpi.com/2032-6653/10/4/84

[4] J. Shin et al., "Design and implementation of shaped magnetic-resonance-based wireless power transfer system for roadway-powered moving electric vehicles," *IEEE Trans. Ind. Electron.*, vol. 61, no. 3, pp. 1179–1192, Mar. 2014.

[5] A. Calabro, B. Cohen, A. Daga, J. Miller, and F. McMahon, "Performance of 200-kW inductive charging system for range extension of electric transit buses," in *Proc. IEEE Transp. Electrific. Conf. Expo (ITEC)*, Jun. 2019, pp. 1–5.

[6] V. Cirimele, M. Diana, F. Freschi, and M. Mitolo, "Inductive power transfer for automotive applications: State-of-the-art and future trends," *IEEE Trans. Ind. Appl.*, vol. 54, no. 5, pp. 4069–4079, Sep. 2018.

[7] C. Beckers, I. Besselink, and H. Nijmeijer, "The state-of-the-art of battery electric city buses," in *Proc. 34th Int. Electr. Vehicle Symp. Exhib. (EVS)*, Nanjing, China, 2021, pp. 25–28.

[8] J. H. Kim et al., "Development of 1-MW inductive power transfer system for a high-speed train," *IEEE Trans. Ind. Electron.*, vol. 62, no. 10, pp. 6242–6250, Oct. 2015.

[9] H. H. Wu and M. P. Masquelier, "An overview of a 50kW inductive charging system for electric buses," in *Proc. IEEE Transp. Electrific. Conf. Expo. (ITEC)*, Jun. 2015, pp. 1–4.

[10] S.-H. Lee, B.-S. Lee, and J.-H. Lee, "A new design methodology for a 300-kW, low flux density, large air gap, online wireless power transfer system," *IEEE Trans. Ind. Appl.*, vol. 52, no. 5, pp. 4234–4242, Sep. 2016.

[11] B. Goeldi, J. Tritschler, and S. Reichert, "Measurement results of a 22 kW bidirectional inductive charger," in *Proc. PCIM Eur. Int. Exhib. Conf. Power Electron., Intell. Motion, Renew. Energy Energy Manage.*, May 2015, pp. 1–8.

[12] M. Bojarski, E. Asa, K. Colak, and D. Czarkowski, "A 25 kW industrial prototype wireless electric vehicle charger," in *Proc. IEEE Appl. Power Electron. Conf. Expo. (APEC)*, Mar. 2016, pp. 1756–1761.

[13] R. Bosshard and J. W. Kolar, "Multi-objective optimization of 50 kW/85 kHz IPT system for public transport," *IEEE J. Emerg. Sel. Topics Power Electron.*, vol. 4, no. 4, pp. 1370–1382, Dec. 2016.

[14] IPT Technology GmbH. (2022). *Wireless Opportunity Charging Buses in Madrid*. Accessed: Oct. 17, 2022. [Online]. Available: https://ipt-technology.com/case-opportunity-charging-madrid/

[15] D. Pehrman, Y. Liu, C. Cui, and X. Huang, "Loss reduction by synchronous rectification in a 50 kW SiC-based inductive power transfer system," in *Proc. IECON 46th Annu. Conf. IEEE Ind. Electron. Soc.*, Oct. 2020, pp. 3907–3912.

[16] M. Mohammad, O. C. Onar, J. L. Pries, V. P. Galigekere, G.-J. Su, and J. Wilkins, "Thermal analysis of a 50 kW three-phase wireless charging system," in *Proc. IEEE Transp. Electrific. Conf. Expo. (ITEC)*, Jun. 2021, pp. 1–6.

[17] M. Mohammad et al., "Sensitivity analysis of an LCC-LCC compensated 20-kW bidirectional wireless charging system for medium-duty vehicles," in *Proc. IEEE Transp. Electrific. Conf. Expo. (ITEC)*, Jun. 2019, pp. 1–7.

[18] M. Mohammad et al., "Bidirectional LCC–LCC-compensated 20-kW wireless power transfer system for medium-duty vehicle charging," *IEEE Trans. Transport. Electrific.*, vol. 7, no. 3, pp. 1205–1218, Sep. 2021.

[19] A. U. Ibrahim, W. Zhong, and M. D. Xu, "A 50-kW three-channel wireless power transfer system with low stray magnetic field," *IEEE Trans. Power Electron.*, vol. 36, no. 9, pp. 9941–9954, Sep. 2021.

[20] W. Shi et al., "Design of a highly efficient 20-kW inductive power transfer system with improved misalignment performance," *IEEE Trans. Transport. Electrific.*, vol. 8, no. 2, pp. 2384–2399, Jun. 2022.

[21] P. A. J. Lawton, F. J. Lin, and G. A. Covic, "Magnetic design considerations for high-power wireless charging systems," *IEEE Trans. Power Electron.*, vol. 37, no. 8, pp. 9972–9982, Aug. 2022.

[22] N. Mirković, L. R. Chamorro, A. Delgado, P. Alou, and M. Vasić, "30 kW bidirectional inductive power transfer charger with intermediate coil for EV applications," *IEEE Trans. Power Electron.*, vol. 39, no. 7, pp. 9007–9024, Jul. 2024.

[23] ABB.(2023). *Abb E-Mobility Charging Solutions for Electric Bus Fleets*. Brochure. [Online]. Available: https://search.abb.com/library/Download.aspx?DocumentID=9AKK108467A8434&LanguageCode=en&DocumentPartId=PDF&Action=Launch

[24] I. Diab, R. Eggermont, G. R. Chandra Mouli, and P. Bauer, "An adaptive battery charging method for the electrification of diesel or CNG buses as in-motion-charging trolleybuses," *IEEE Trans. Transport. Electrific.*, vol. 9, no. 3, pp. 4531–4540, Sep. 2023.

[25] D. Smith et al., "Medium- and heavy-duty vehicle electrification: An assessment of technology and knowledge gaps," Oak Ridge Nat. Lab. (ORNL), Oak Ridge, TN, USA, Tech. Rep. ORNL/SPR-2020/7, 2020.

[26] S. Bandyopadhyay, P. Venugopal, J. Dong, and P. Bauer, "Comparison of magnetic couplers for IPT-based EV charging using multi-objective optimization," *IEEE Trans. Veh. Technol.*, vol. 68, no. 6, pp. 5416–5429, Jun. 2019.

[27] C. de la Garza Cuevas, "Electromagnetic field modeling for the charging pads of a 50 kw IPT system and mechanical design for the pad's casings," Delft Univ. Technol., Delft, The Netherlands, Tech. Rep. b59807bc-27f1-46e8-a437-0182e32428ab, Aug. 2022.

[28] Z. Luo, X. Wei, M. G. S. Pearce, and G. A. Covic, "Multiobjective optimization of inductive power transfer double-D pads for electric vehicles," *IEEE Trans. Power Electron.*, vol. 36, no. 5, pp. 5135–5146, May 2021.

[29] J. Deng, Y. Zhang, S. Wang, Z. Wang, and Y. Yang, "The design and coupler optimization of a single-transmitter coupled multireceiver inductive power transfer system for Maglev trains," *IEEE Trans. Transport. Electrific.*, vol. 7, no. 4, pp. 3173–3184, Dec. 2021.

[30] T. Kuruoglu, "Opportunity charging: A case study based on real-life public transportation scenarios," Delft Univ. Technol., Delft, The Netherlands, Tech. Rep. f41b51ec-0c90-4537-8b00-af7018e20400, Jun. 2023, pp. 1–54.

[31] Wireless Power Transfer for Heavy-Duty Electric Vehicles, Standard J2954RP, SAE International, Dec. 2022.

[32] W. Li, H. Zhao, J. Deng, S. Li, and C. C. Mi, "Comparison study on SS and double-sided LCC compensation topologies for EV/PHEV wireless chargers," *IEEE Trans. Veh. Technol.*, vol. 65, no. 6, pp. 4429–4439, Jun. 2016.
[33] R. Bosshard, J. W. Kolar, J. Mühlethaler, I. Stevanovic, B. Wunsch, and F. Canales, "Modeling and η-α-Pareto optimization of inductive power transfer coils for electric vehicles," *IEEE J. Emerg. Sel. Top. Power Electron.*, vol. 3, no. 1, pp. 50–64, Mar. 2015.
[34] J. Mühlethaler, "Modeling and multi-objective optimization of inductive power components," Ph.D. dissertation, Power Electron. Syst. Lab., Swiss Federal Inst. Technol. Zurich, ETHZ, Zürich, The Switzerland, 2012.
[35] (2015). *3C95 Material Specification*. Ferroxcube. [Online]. Available: https://www.ferroxcube.com/upload/media/product/file/MDS/3c95.pdf
[36] (2008). *Soft Ferrites: Ferrites Mateiral Survey*. Ferroxcube. [Online]. Available: https://ferroxcube.home.pl/prod/assets/sfmatgra frnt.pdf
[37] R. P. Feynman, R. B. Leighton, and M. Sands. (2013). *The Feynman Lectures on Physics, Volume II Chapter 23*. [Online]. Available: https://www.feynmanlectures.caltech.edu/II_23.html
[38] F. Kreuger. (1995). *Industrial High DC Voltage 1. Fields, 2. Breakdowns, 3. Tests*. [Online]. Available: https://resolver.tudelft.nl/uuid: bf4186ec-d67a-4438-871b-ecadf7c59531
[39] Y. del Valle, G. K. Venayagamoorthy, S. Mohagheghi, J.-C. Hernandez, and R. G. Harley, "Particle swarm optimization: Basic concepts, variants and applications in power systems," *IEEE Trans. Evol. Comput.*, vol. 12, no. 2, pp. 171–195, Apr. 2008.
[40] BYD. (2019). *The Byd K9s*. Accessed: Jul. 28, 2022. [Online]. Available: https://en.byd.com/wp-content/uploads/2019/07/4504-byd-transit-cut-sheets_k9s-35_lr.pdf

Calvin Riekerk (Graduate Student Member, IEEE) received the B.S. and M.S. degrees in electrical engineering from Delft University of Technology (TU Delft), Delft, The Netherlands, in 2018 and 2020, respectively, where he is currently pursuing the Ph.D. degree in wireless power transfer.

He is a System Engineer with Nederlandse Spoorwegen (NS), TU Delft. His research interests include power electronics and wireless charging.

Mr. Riekerk was a recipient of the IEEE Best High Tech Start-up Business Plan in 2018.

Wenli Shi (Member, IEEE) received the Ph.D. degree in electrical engineering from Delft University of Technology (TU Delft), Delft, The Netherlands, in 2023.

In March 2023, he started working as a Post-Doctoral Researcher at the DC System, Energy Conversion and Storage (DCE&S) Group, TU Delft. Since May 2024, he has been an Assistant Professor at the DCE&S Group. His research interests include high-power wireless charging, dc power distribution systems, and dc circuit breakers.

Dr. Shi serves as an Associate Editor for IEEE TRANSACTIONS ON TRANSPORTATION ELECTRIFICATION and the Vice-Chair of IEEE BENELUX SECTION TRANSPORTATION ELECTRIFICATION COUNCIL.

Gangwei Zhu (Member, IEEE) received the B.S. degree in electrical engineering from Central South University, Changsha, China, in 2018, the M.S. degree in electrical engineering from Shanghai Jiao Tong University, Shanghai, China, in 2021, and the Ph.D. degree in electrical engineering from Delft University of Technology (TU Delft), Delft, The Netherlands, in 2024.

He is currently a Post-Doctoral Research Fellow with the City University of Hong Kong, Hong Kong. His research interests include design, modeling, and control for power electronics and wireless power transfer.

Dr. Zhu was a recipient of the IEEE Transportation Electrification Council (TEC) Ph.D. Thesis Talk Prize, the Best Paper Award (First Place) at the IEEE International Zhejiang Power Electronics Conference (ZPEC), and the IEEE Industrial Electronics Society (IES) Student and Young Professionals Paper Assistance (SYPA) Award.

Jianning Dong (Senior Member, IEEE) received the B.S. and Ph.D. degrees in electrical engineering from Southeast University, Nanjing, China, in 2010 and 2015, respectively.

He was a Post-Doctoral Researcher with the McMaster Automotive Resource Centre, McMaster University, Hamilton, ON, Canada. He has been an Assistant Professor since 2016 and an Associate Professor since 2025 with the DC System, Energy Conversion and Storage (DCE&S) Group, Delft University of Technology (TU Delft), Delft, The Netherlands. His research interests include electromechanical energy conversion and contactless power transfer.

Thiago Batista Soeiro (Senior Member, IEEE) received the Ph.D. degree in electrical engineering from the Swiss Federal Institute of Technology, ETH Zürich, Zürich, Switzerland, in 2012.

From 2013 to 2018, he worked at the Corporate Research Center, ABB Switzerland Ltd., Turgi, Switzerland. From 2018 to 2022, he worked as an Associate Professor with the DC Systems, Energy Conversion, and Storage Group, Delft University of Technology (TU Delft), Delft, The Netherlands. In 2022, he worked at the European Space Research and Technology Centre, Noordwijk, The Netherlands. Since 2022, he has been a Full Professor and the Head of the Power Electronics Group, University of Twente, Enschede, The Netherlands.

Pavol Bauer (Senior Member, IEEE) is currently a Full Professor with the Department of Electrical Sustainable Energy, Delft University of Technology (TU Delft), Delft, The Netherlands, and the Head of the DC Systems, Energy Conversion and Storage Group. From 2002 to 2003, he was working partially at KEMA (DNV GL, Arnhem) on different projects related to power electronics applications in power systems. He published over 180 journal papers and over 500 conference papers in his field (with H factor Google Scholar 65, Web of Science 43), he is an author or co-author of eight books, holds ten international patents, and organized several tutorials at the international conferences. He has worked on many projects for industry concerning wind and wave energy, power electronic applications for power systems such as Smarttrafo; HVdc systems, projects for smart cities such as PV charging of electric vehicles, PV and storage integration, contactless charging; and he participated in several Leonardo da Vinci, H2020 and Electric Mobility Europe EU projects as project partner (ELINA, INETELE, E-Pragmatic, Micact, Trolley 2.0, OSCD, P2P, Progressus, Tulip, and Flow) and coordinator (PEMCWebLab.com-Edipe, SustEner, and Eranet DCMICRO). His main research interest is power electronics for charging of electric vehicles and dc grids.

Dr. Bauer is a member of the Executive Committee of the European Power Electronics Association (EPE) and a member of the international steering committee at numerous conferences. He is the former Chair of Benelux IEEE Joint Industry Applications Society, Power Electronics and Power Engineering Society chapter, the Chair of the Power Electronics and Motion Control (PEMC) council, and the Chair of Benelux IEEE Industrial Electronics chapter.